
Shock-Ignition Experiments with Planar Targets on OMEGA

In inertial confinement fusion (ICF), a capsule containing cryogenic deuterium–tritium fusion fuel is rapidly compressed to high temperatures and areal densities sufficient for thermonuclear fusion. If the α particles generated via D–T fusion reactions in the central hot spot of an imploded capsule deposit their energy in the compressed core, the capsule ignites. Provided the confinement time determined by the fuel-mass inertia is sufficiently long, the energy released via the fusion burn can exceed the incident driver energy and the fusion gain exceeds unity. The demonstration of this concept is the main goal of ICF research.¹ In laser-driven ICF the compression drive is provided by coupling laser energy into an ablator surrounding a spherical fuel capsule, either directly through symmetric irradiation of the fusion target or indirectly via a thermal x-ray bath generated from laser illumination of the inner walls of a cavity (hohlraum). In the shock-ignition (SI) concept,² the fuel-assembly and ignition stages are separated by using shaped, nanosecond laser pulses. During the compression stage of the laser, the fuel is assembled to a high areal density (ρR) at sub-ignition velocity, resulting in a central hot-spot temperature insufficient for ignition. A high-intensity laser spike at the end of the assembly pulse then launches a strong shock wave, the timing of which is such that the return shock, caused by the rising hot-spot pressure, collides with the strong shock inside the fuel.³ This results in two new shocks, one of which propagates inward, heating and compressing the hot spot to ignition conditions and causing a *non-isobaric* pressure profile peaked at the center. This is energetically favorable compared to the *isobaric* distribution in conventional hot-spot ignition, where both hot spot and fuel are compressed to the same pressure p_{iso} , and is a key advantage of shock ignition. It can be shown that the energy required to achieve shock ignition decreases as $\sim(p/p_{\text{iso}})^3$, where the non-isobaric hot-spot pressure p directly depends on the initial laser-driven shock strength at the ablator and its amplification through spherical convergence in the fuel.⁴

Taking full advantage of the SI scheme requires laser-generated shocks at the ablator of ~ 300 -Mbar, launched in the presence of a long-scale-length pre-plasma generated by the assembly laser pulse. For such strong shocks, on-target inten-

sities exceeding 10^{15} W/cm² are necessary and laser–plasma instabilities (LPI’s) play an important role in the coupling of laser energy to the target. These lead to energy losses through stimulated Raman and Brillouin scattering (SRS and SBS, respectively) and hot-electron generation and potential fuel preheat by fast electrons produced through SRS and two-plasmon decay. Hot electrons are predominantly generated by the laser spike late in the target evolution when the areal density grows rapidly. Provided the electron stopping distance is within the shell thickness, they can even augment the ignitor shock strength and enhance the target performance.⁵

The idea of separating fuel assembly and ignition is conceptually similar to fast ignition.⁶ For SI, however, complicated cone-in-shell targets are not necessary, and SI can use the pulse-shaping capabilities of existing facilities designed for hot-spot ignition rather than requiring an additional short-pulse, multipetawatt ignitor laser. This significantly relaxes the technical and financial constraints on fielding this concept experimentally or in a fusion-energy context.

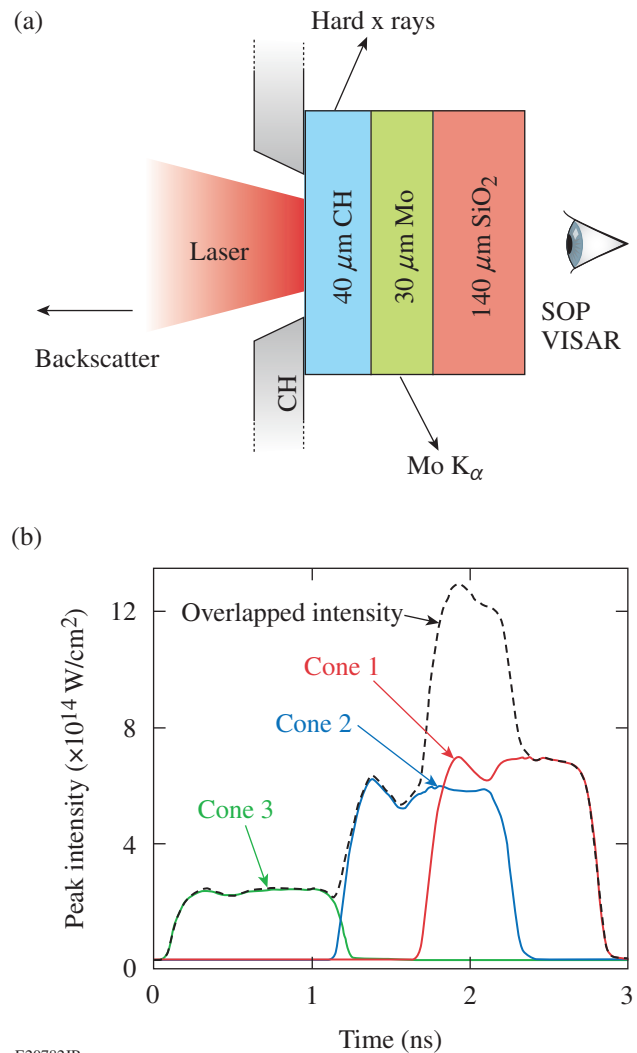
SI has received considerable attention as an alternative path to ignition, e.g., for the National Ignition Facility,⁷ HiPER,⁸ and the LMJ project.⁹ Theoretical studies have investigated target design and robustness,¹⁰ but only a few experimental studies have been performed. Preliminary work on the OMEGA Laser System¹¹ using warm, spherical plastic targets driven by a SI-type laser pulse showed $\sim 30\%$ higher ρR , larger neutron yields, and better implosion stability than hydrodynamic- and energy-equivalent implosions without a high-intensity shock spike.⁴

This article presents experimental results on LPI and laser-driven shock propagation in planar geometry and at SI-relevant intensities performed using OMEGA. To infer initial shock properties, the data are compared to two-dimensional (2-D) radiative–hydro–dynamic simulations that show very good agreement with the experiment. Based on the numerical results, the experiment discussed here represents the first demonstration of a laser-driven, 70-Mbar shock in the presence of a long-scale-length pre-plasma.

Figure 131.1(a) shows a schematic of the experimental setup. The planar targets consisted of three layers: a 40- μm plastic ablator onto which the laser was focused, followed by 30 μm of Mo and 140 μm of SiO_2 . The Mo was used to shield hot electrons from propagating into the final layer and to infer the hot-electron population through time-integrated recording of the Mo- K_α emission with an absolutely calibrated x-ray spectrometer. The final SiO_2 layer was used to observe the shock temperature through streaked optical pyrometry (SOP)¹² and the shock propagation via two VISAR (velocity interferometer system for any reflector) diagnostics with different velocity responses (10.4 and 6.4 $\mu\text{m}/\text{ns}/\text{fringe}$) (Ref. 13). Since the Mo is opaque to optical wavelengths, the laser-driven shock could be observed only after entering the SiO_2 layer. The quartz also acted as a “get-lost” layer that prevented refluxing of hot electrons in the Mo. In addition, a CH washer was attached to the front of the target to stop diffracted laser light from hitting the target’s sides and to stop electrons from streaming around the target. Further diagnostics included a four-channel, time-resolved, hard x-ray detector that measured the hot-electron temperature¹⁴ and backscattering diagnostics that determined SRS and SBS levels within the focal cone of two beams in the strong-shock drive as well as one location between two strong-shock beams.¹⁵

Figure 131.1(b) shows an example for the temporal on-target intensity profile of the 351-nm-wavelength laser light at the position of the unperturbed target surface. With an on-target energy between ~ 5 kJ and 7.2 kJ, the total irradiation profile [dashed line in Fig. 131.1(b)] was achieved by stacking three laser cones in time with individual focusing parameters. Beam smoothing was achieved with polarization smoothing¹⁶ and distributed phase plates (DPP’s).¹⁷ Beams in Cones 2 and 3 (blue and green, respectively) were focused to a $1/e$ intensity radii of 412 μm and 310 μm , respectively, using “SG8” and defocused “SG4” DPP’s. These two cones formed a pre-plasma for ~ 1.6 ns, while the overlap between Cones 1 (red) and 2 provided the high-intensity spike driving a strong shock into the target. Beams in Cone 1 were focused to a 302- μm radius using defocused “IDI300” DPP’s. Cone 3 consisted of eight beams at an incidence angle of 62.3°; Cones 1 and 2 comprised six spatially overlapping beams at 23.4° and 47.8°, respectively. While Cones 2 and 3, and therefore the pre-plasma conditions, were kept the same throughout the experiment, the energy contained in Cone 1 was varied to give an overlapped “spike intensity” ranging from ~ 0.6 to 1.4×10^{15} W/cm^2 .

Results for the hot-electron temperature and population as a function of the nominal spike intensity are displayed in

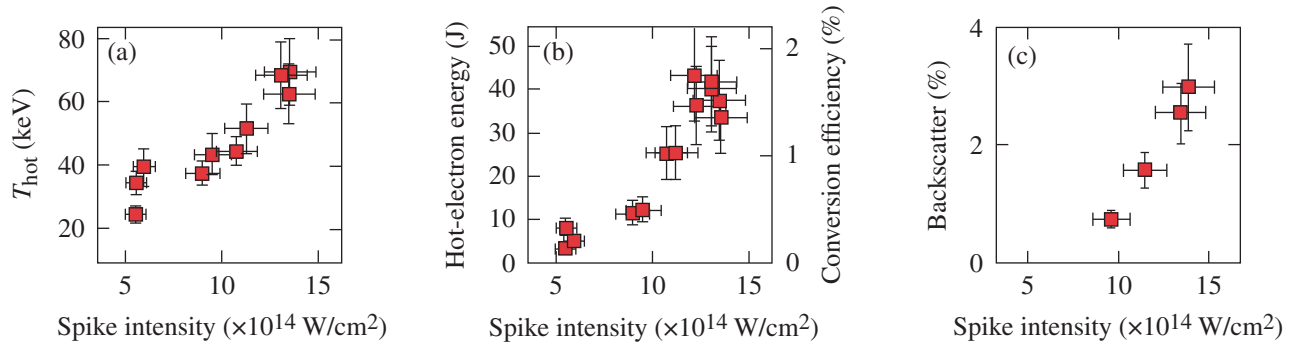


E20782JR

Figure 131.1

(a) Schematic of the planar target driven by a laser pulse as shown in (b). The pulse was generated by stacking three laser cones in time and space, each with its own energy and focusing parameters. SOP: streaked optical pyrometry; VISAR: velocity interferometer system for any reflector.

Fig. 131.2. The electron temperature [Fig. 131.2(a)] rises with intensity, indicating an increase in LPI, and reaches a peak of ~ 70 keV at the highest-intensity case considered here. The total energy in the hot-electron component [Fig. 131.2(b)] was inferred from comparing the time-integrated Mo- K_α yield to Monte Carlo simulations.¹⁸ The emission of hard x rays was strongly correlated to the high-intensity spike of the drive laser. Therefore, the hot-electron conversion efficiency, plotted on the right y axis of Fig. 131.2(b), is given by comparing the energy contained in the hot-electron component to that in the laser spike, i.e., the energy incident on target during the overlap between Cones 1 and 2. As expected, it increased with



E20783JR

Figure 131.2

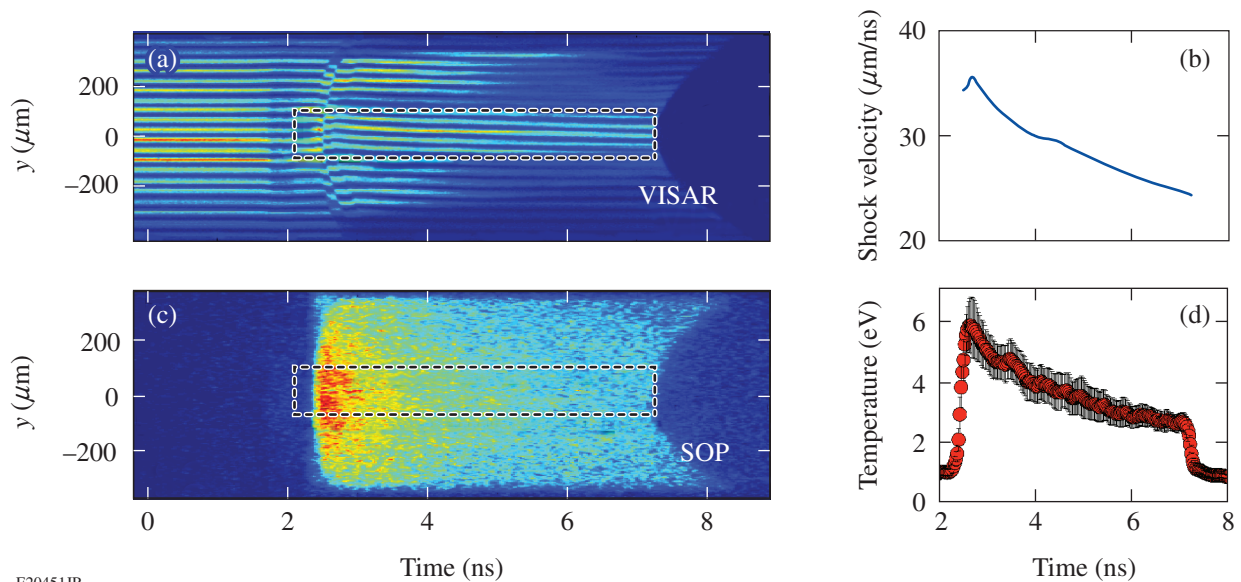
(a) Hot-electron temperature as a function of peak laser intensity; (b) laser conversion efficiency and total energy contained in the hot-electron component; (c) fraction of backscattered laser energy (SRS + SBS) within the strong-shock beam cones as a function of peak intensity.

rising intensity, and at the highest intensity, 1.8% of the spike energy was converted to hot electrons. The error bars in these data are dominated by the precision of the measured K_{α} yield ($\sim 25\%$) (Ref. 18).

Results for the backscattered laser light (SRS and SBS) within the shock-beam focal cones are plotted as a function of peak intensity in Fig. 131.2(c). This also increased with incident intensity, reaching $\sim 3\%$ for the highest-intensity case. Sidescatter was also observed but was not fully quantified and

is not included in Fig. 131.2(c). Since the light reflection is nonuniform, and there are too few diagnostics to infer a full scattering profile, so the interpretation of the data with respect to a total backscattered energy in these planar experiments is difficult. The sidescatter is not expected to exceed the in-beam scattering, giving an upper limit for the total amount of scattered light of $\sim 10\%$ at 1.4×10^{15} W/cm².

Examples for shock-evolution data obtained with VISAR and SOP diagnostics are shown in Figs. 131.3(a) and 131.3(c),



E20451JR

Figure 131.3

Experimental shock-propagation data obtained with (a) VISAR and (c) SOP at a peak intensity of 9×10^{14} W/cm²; (b) and (d) show extracted shock velocity and temperature, respectively.

respectively. These data were taken with a spike intensity of $\sim 9 \times 10^{14}$ W/cm², and all figures are plotted as a function of time with $t = 0$ corresponding to the onset of the laser pulse [see Fig. 131.1(b)]. The slight drop in signal strength of the VISAR data at ~ 1.7 ns is caused by the laser spike hitting the target. This results in the generation of hot electrons, some of which reach the SiO₂ layer and alter the refractive index of the material through ionization, causing partial absorption of the probe laser. Since the Mo layer is opaque, no shock front can be observed until its breakout from the Mo into the SiO₂ at ~ 2.5 ns. This causes a strong fringe shift in the VISAR and a signal onset in the SOP. The subsequent slowly varying fringe shift in Fig. 131.3(a) is indicative of a decelerating shock. At ~ 7.2 ns the shock breaks out into vacuum through the rear of the target, as evidenced by the pronounced signal drop in both data sets. The shock is strongest and fastest in the center, where the drive laser's intensity is at its peak, and edge rarefactions cause a strong curvature of the shock front and the breakout feature. These data can be used to extract a shock velocity in the range of 30 $\mu\text{m}/\text{ns}$ [Fig. 131.3(b)] and an emission temperature of a few eV [Fig. 131.3(d)] inside the SiO₂ layer.

The incident laser pulse launched multiple shocks into a target, but the primary goal was to characterize the strong shock driven by the high-intensity spike. The conditions inside the ablator cannot be observed directly. Instead, the strong shock's initial conditions were inferred by matching numerical

simulation results to the experimental data. For this purpose the 2-D radiative hydrocode *DRACO* was used¹⁹ Note that a 2-D treatment is strictly necessary as evidenced by the curvature of the rear shock-breakout feature in Figs. 131.3(a) and 131.3(c). Figure 131.4 shows snapshots of the pressure distribution from a simulation using the experimental conditions for the data in Fig. 131.3. The x axis denotes the target's thickness; the y axis is the lateral extent of the target. The simulations assumed azimuthal symmetry and $y = 0$ corresponds to the point of peak laser intensity. The laser drives the target from the left and the shocks propagate to the right. A schematic of the initial target layout is shown at the top of Fig. 131.4(a), and the dashed lines indicate unperturbed interface positions.

At 2.5 ns [Fig. 131.4(a)] the foremost shock reaches the Mo/SiO₂ interface, which agrees well with the data in Fig. 131.3. At this time, ~ 200 ps after the end of the high-intensity drive, the strong shock is already starting to decrease in strength and has almost caught up with the weaker shock generated by the pre-plasma laser pulse. This is also in good agreement with the VISAR data, which exhibit two subsequent fringe jumps within ~ 100 ps: the first upon the breakout of the pre-plasma shock into the SiO₂ layer, quickly followed by the coalescence with the trailing strong shock. At 7.1 ns of the simulated target evolution [Fig. 131.4(b)], the shock front reaches the target/vacuum interface at the rear, also agreeing very well with the experimental data, which exhibit this event at 7.2 ns.

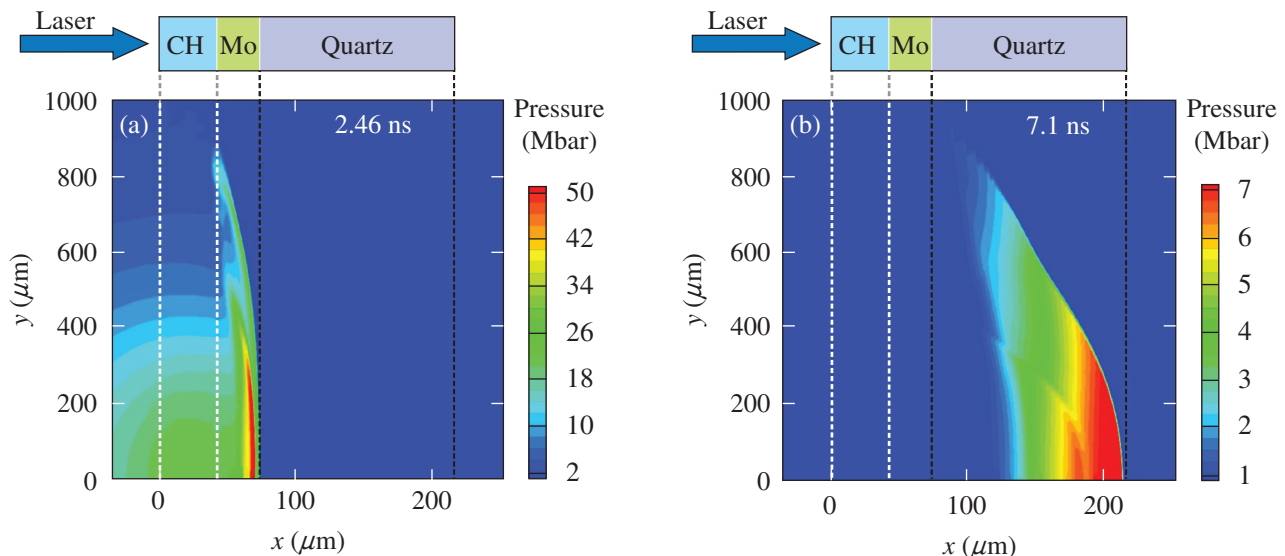


Figure 131.4

Snapshots of the pressure distribution at (a) 2.46 ns and (b) 7.1 ns from *DRACO* simulations using the experimental conditions for the data in Fig. 131.3. A schematic of the initial target layout is shown above (a) and (b). The dashed lines indicate initial interface positions.

The simulated target evolution is reproduced well over the range of intensities used in the experiment. Figure 131.5(a) shows the rear shock-breakout time as a function of spike intensity, with the squares denoting experimental data and the circles numerical results. The lowest-intensity case corresponds to no energy in Cone 1, i.e., no laser spike is incident on the target. The agreement between the simulated shock-propagation time to the experimentally measured one is better than 5% over the full intensity range, indicating a good numerical treatment of the laser–target interaction and ablator physics.

To extract the ablatively driven shock strength in the plastic layer from these simulations, the impedance mismatch between the plastic and Mo needs to be taken into account. The heavier Mo causes a partial shock reflection that overlaps with the laser-driven one, leading to an increase of the observed strong-shock strength in the ablator at the time of peak intensity. The purely ablatively driven shock strength was inferred through simulations using the same laser conditions, but an all-CH target. This results in a reduction of $\sim 25\%$ in the peak pressure, when compared to the CH/Mo/SiO₂ targets. The simulated ablation pressures corrected for the impedance mismatch are plotted as the blue circles in Fig. 131.5(b). The simulation results provide a scale relating shock propagation and ablation pressure, which was then used to infer ablation pressures via the experimentally observed shock-propagation time [red squares in Fig. 131.2(b)]. The error bars for the numerical results reflect temporal variations of the simulated pressure. This, in addition to the experimental uncertainty in the shock-propagation time, determines the error for the inferred pressures. Based on these results, a peak ablation pressure of ~ 70 Mbar was achieved with a drive intensity of $\sim 1.2 \times 10^{15}$ W/cm² in the presence of a long-scale-length pre-plasma. The simulated plasma density scale length at quarter-critical in these experiments is ~ 350 μm at the time of the high-intensity spike, with coronal temperatures between 2.0 keV and 2.9 keV, depending on the spike intensity. This compares well to previous experimental and numerical results for laser intensities of mid- 10^{14} W/cm² (Refs. 18 and 20) but is lower than expected for a NIF-scale shock-ignition target (~ 450 μm , ~ 8 keV). The scale length in these experiments is limited by the focal-spot size, and the temperature by the spike intensity.

In Ref. 21 the stationary ablation pressure in a pure plastic target was derived to be $p_a = 40 (I_{15} / \lambda_{\mu\text{m}})^{2/3}$, where I_{15} denotes the absorbed laser intensity in units of 10^{15} W/cm² and $\lambda_{\mu\text{m}}$ is the laser wavelength in microns. The absorption fraction of the high-intensity spike observed in the simulations is typically $\sim 90\%$. The simulations do not include hot electrons,

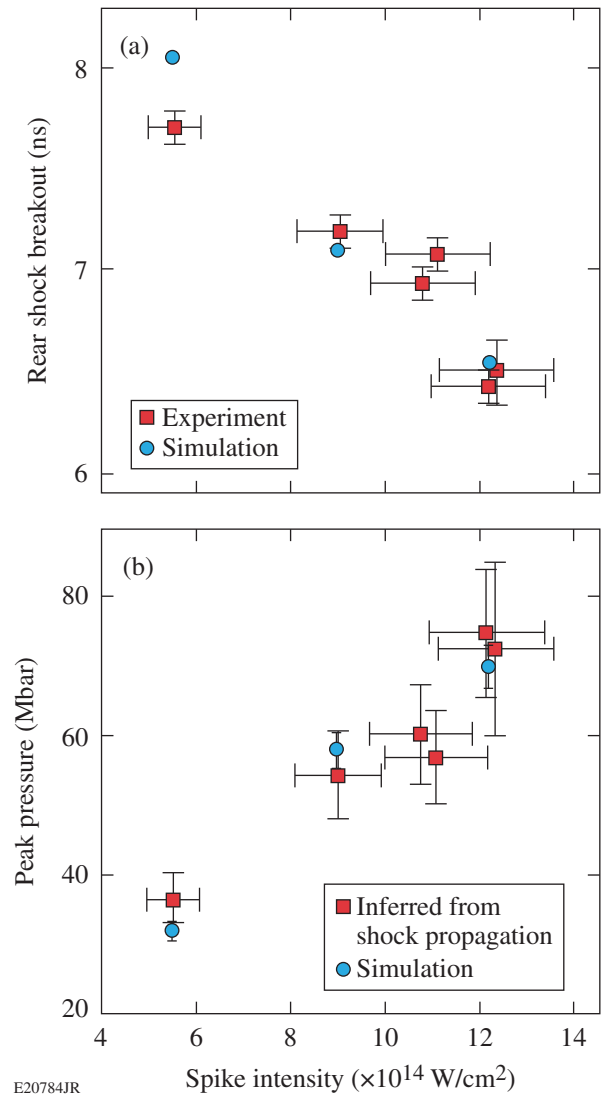


Figure 131.5 (a) Simulated (circles) and experimental (squares) shock-propagation time as a function of peak intensity; (b) laser-driven ablation pressure inferred from all-CH target simulations as a function of peak intensity.

but this contributes, at most, a few percent [Fig. 131.2(b)], and the agreement between simulated and observed target evolution gives confidence in the numerical treatment of the laser–target interaction. Applying the numerical absorption fraction to the pressure scaling overestimates the ablation pressure by 20% to 50%. This mismatch is not surprising since the pressure scaling makes the simplified assumption that laser absorption is limited to the critical surface, and therefore cannot be expected to capture the absorption physics correctly.

The simulations may be used to calculate the expected target conditions at full shock-ignition intensities. With a spike

intensity of $\sim 10^{16}$ W/cm², pressures of ~ 300 Mbar should be achieved for a simulated 70% absorption of the high-intensity spike—sufficient to drive a shock-ignition experiment. As before, the simulations do not include a treatment of hot electrons, and whether this extrapolation is valid needs to be investigated. The impact of the hot-electron component on the strong-shock strength is still under investigation and will depend on the temperature of the electron distribution.⁵ Clearly, more experiments are required to characterize the plasma and shock conditions at such high intensities.

In conclusion, experiments investigating shock strength and the impact of LPI at SI-relevant laser conditions have been performed. Planar targets were irradiated with laser pulses comprising a pre-plasma—generating foot and a high-intensity spike to launch a strong shock. At a peak intensity of 1.4×10^{15} W/cm², an electron temperature of 70 keV was measured with $\sim 1.8\%$ of the spike energy being converted to hot electrons, and $\leq 10\%$ of the laser energy was scattered. Simulations using the radiative 2-D hydrocode *DRACO* show very good agreement with the observed shock propagation. Based on these results, at an intensity of 1.2×10^{15} W/cm², a 70-Mbar shock was generated in the presence of a 350- μ m pre-plasma. This is the highest pressure reported at SI-relevant conditions, and these experiments constitute an important step toward validating the shock-ignition concept experimentally.

ACKNOWLEDGMENT

This work has been supported by the U.S. Department of Energy under Cooperative Agreement Nos. DE-FC02-04ER54789 and DE-FC52-08N28302, the University of Rochester, and the New York State Energy Research and Development Authority. The support of DOE does not constitute an endorsement by DOE of the views expressed in this article. We acknowledge useful discussions with P. M. Celliers.

REFERENCES

1. S. Atzeni and J. Meyer-ter-Vehn, *The Physics of Inertial Fusion: Beam Plasma Interaction, Hydrodynamics, Hot Dense Matter*, International Series of Monographs on Physics (Clarendon Press, Oxford, 2004).
2. R. Betti, C. D. Zhou, K. S. Anderson, L. J. Perkins, W. Theobald, and A. A. Solodov, *Phys. Rev. Lett.* **98**, 155001 (2007).
3. R. Nora and R. Betti, *Phys. Plasmas* **18**, 082710 (2011).
4. W. Theobald, R. Betti, C. Stoeckl, K. S. Anderson, J. A. Delettrez, V. Yu. Glebov, V. N. Goncharov, F. J. Marshall, D. N. Maywar, R. L. McCrory, D. D. Meyerhofer, P. B. Radha, T. C. Sangster, W. Seka, D. Shvarts, V. A. Smalyuk, A. A. Solodov, B. Yaakobi, C. D. Zhou, J. A. Frenje, C. K. Li, F. H. Séguin, R. D. Petrasso, and L. J. Perkins, *Phys. Plasmas* **15**, 056306 (2008).
5. R. Betti, W. Theobald, C. D. Zhou, K. S. Anderson, P. W. McKenty, S. Skupsky, D. Shvarts, V. N. Goncharov, J. A. Delettrez, P. B. Radha, T. C. Sangster, C. Stoeckl, and D. D. Meyerhofer, *J. Phys., Conf. Ser.* **112**, 022024 (2008).
6. M. Tabak *et al.*, *Phys. Plasmas* **1**, 1626 (1994).
7. L. J. Perkins, R. Betti, K. N. LaFortune, and W. H. Williams, *Phys. Rev. Lett.* **103**, 045004 (2009).
8. X. Ribeyre *et al.*, *Plasma Phys. Control. Fusion* **51**, 015013 (2009).
9. B. Canaud and M. Temporal, *New J. Phys.* **12**, 043037 (2010).
10. S. Atzeni, A. Schiavi, and A. Marocchino, *Plasma Phys. Control. Fusion* **53**, 035010 (2011); O. Klimo *et al.*, *Phys. Plasmas* **18**, 082709 (2011); M. Lafon, X. Ribeyre, and G. Schurtz, *Phys. Plasmas* **17**, 052704 (2010); X. Ribeyre *et al.*, *ibid.* **18**, 102702 (2011); C. Riconda *et al.*, *ibid.* **18**, 092701 (2011); A. J. Schmitt *et al.*, *ibid.* **17**, 042701 (2010).
11. T. R. Boehly, D. L. Brown, R. S. Craxton, R. L. Keck, J. P. Knauer, J. H. Kelly, T. J. Kessler, S. A. Kumpan, S. J. Loucks, S. A. Letzring, F. J. Marshall, R. L. McCrory, S. F. B. Morse, W. Seka, J. M. Soures, and C. P. Verdon, *Opt. Commun.* **133**, 495 (1997).
12. J. E. Miller, T. R. Boehly, A. Melchior, D. D. Meyerhofer, P. M. Celliers, J. H. Eggert, D. G. Hicks, C. M. Sorce, J. A. Oertel, and P. M. Emmel, *Rev. Sci. Instrum.* **78**, 034903 (2007).
13. P. M. Celliers, D. K. Bradley, G. W. Collins, D. G. Hicks, T. R. Boehly, and W. J. Armstrong, *Rev. Sci. Instrum.* **75**, 4916 (2004).
14. C. Stoeckl, V. Yu. Glebov, D. D. Meyerhofer, W. Seka, B. Yaakobi, R. P. J. Town, and J. D. Zuegel, *Rev. Sci. Instrum.* **72**, 1197 (2001).
15. W. Seka, D. H. Edgell, J. P. Knauer, J. F. Myatt, A. V. Maximov, R. W. Short, T. C. Sangster, C. Stoeckl, R. E. Bahr, R. S. Craxton, J. A. Delettrez, V. N. Goncharov, I. V. Igumenshchev, and D. Shvarts, *Phys. Plasmas* **15**, 056312 (2008).
16. T. R. Boehly, V. A. Smalyuk, D. D. Meyerhofer, J. P. Knauer, D. K. Bradley, R. S. Craxton, M. J. Guardalben, S. Skupsky, and T. J. Kessler, *J. Appl. Phys.* **85**, 3444 (1999).
17. Y. Lin, T. J. Kessler, and G. N. Lawrence, *Opt. Lett.* **20**, 764 (1995).
18. B. Yaakobi, P.-Y. Chang, A. A. Solodov, C. Stoeckl, D. H. Edgell, R. S. Craxton, S. X. Hu, J. F. Myatt, F. J. Marshall, W. Seka, and D. H. Froula, *Phys. Plasmas* **19**, 012704 (2012).
19. P. B. Radha, V. N. Goncharov, T. J. B. Collins, J. A. Delettrez, Y. Elbaz, V. Yu. Glebov, R. L. Keck, D. E. Keller, J. P. Knauer, J. A. Marozas, F. J. Marshall, P. W. McKenty, D. D. Meyerhofer, S. P. Regan, T. C. Sangster, D. Shvarts, S. Skupsky, Y. Srebro, R. P. J. Town, and C. Stoeckl, *Phys. Plasmas* **12**, 032702 (2005).
20. D. H. Froula, B. Yaakobi, S. X. Hu, P.-Y. Chang, R. S. Craxton, D. H. Edgell, R. Follett, D. T. Michel, J. F. Myatt, W. Seka, R. W. Short, A. Solodov, and C. Stoeckl, *Phys. Rev. Lett.* **108**, 165003 (2012).
21. J. D. Lindl, *Phys. Plasmas* **2**, 3933 (1995).